



Mechanism analysis of pitting induced by Al₂O₃ inclusions: insight from simulation calculation

Ting Wang¹ · Bi-jun Hua¹ · Xiang-jun Liu¹ · Pei-hong Yang² · Xiao-xia Shi³ · Ji-chun Yang¹ · Li Zhou¹ · Chang-qiao Yang¹

Received: 7 February 2024 / Revised: 6 May 2024 / Accepted: 15 May 2024
© China Iron and Steel Research Institute Group Co., Ltd. 2024

Abstract

The micro-area characterization experiments like scanning Kelvin probe force microscope (SKPFM) and Kernel average misorientation have the defects of complex sample preparation and occasional errors in test results, which makes it impossible to accurately and quickly analyze the pitting behavior induced by inclusions in some cases, prompting attempts to turn to simulation calculation research. The method of calculating band structure and work function can be used to replace current-sensing atomic force microscopy and SKPFM to detect the potential and conductivity of the sample. The band structure results show that Al₂O₃ inclusion is an insulator and non-conductive, and it will not form galvanic corrosion with the matrix. Al₂O₃ inclusion does not dissolve because its work function is higher than that of the matrix. Moreover, the stress concentration of the matrix around the inclusion can be characterized by first-principles calculation coupled with finite element simulation. The results show that the stress concentration degree of the matrix around Al₂O₃ inclusion is serious, and the galvanic corrosion is formed between the high and the low stress concentration areas, which can be used to explain the reason of the pitting induced by Al₂O₃ inclusions.

Keywords Pitting · Inclusion phase identification · First-principles calculation · Phonopy · Finite element analysis

1 Introduction

At present, about 1/10 of the steels turn into rust each year, causing huge economic losses [1, 2]. Pitting is a very typical localized corrosion, and non-metallic inclusions are an important cause of pitting in steel. It is well known that the onset of pitting is considered to be random and unpredictable. At this stage, the exploration of pitting

mainly focuses on the two thermodynamic categories of voltaic potential difference [3–5] and stress concentration phenomenon [6–8].

Pitting occurs mainly due to the presence of electrochemical nonuniformity between non-metallic inclusions and the adjacent matrix. The characterization of the microscopic electrochemical properties of inclusions in steel is complex. At present, the scanning Kelvin probe force microscope (SKPFM) has been used to characterize the electrochemical activity of inclusions and matrix in most studies [9, 10]. However, the commercial SKPFM has a resolution of only 10 nm in a vacuum environment. The poor spatial resolution may make the experiment inaccurate. Liu et al. [11] measured by SKPFM that the potential of (RE)AlO₃ inclusion is higher than that of the matrix. In theory, the lower the potential, the more likely to suffer corrosion, so that the matrix should be dissolved first. However, immersion experiments showed that (RE)AlO₃ inclusion was dissolved. Obviously, SKPFM may not work for (RE)AlO₃ inclusion. Bettini et al. [12] also found a similar phenomenon when SKPFM was used to detect the

✉ Xiang-jun Liu
liuxiangjun2014@yeah.net

✉ Chang-qiao Yang
yangchangqiao@21cn.com

¹ School of Rare Earth Industry, Inner Mongolia University of Science and Technology, Baotou 014010, Inner Mongolia, China

² School of Automation and Electrical Engineering, Inner Mongolia University of Science and Technology, Baotou 014010, Inner Mongolia, China

³ Inner Mongolia Baotou Steel Union Co., Ltd., Baotou 014010, Inner Mongolia, China

potentials of Cr₂N, ferrite and austenite, and the detection results were inconsistent with the results of immersion experiments. In addition, Xue et al. [13] pointed out that TiN inclusion has a lower potential than Fe matrix by SKPFM test, and it acts as a cathode during the galvanic corrosion process. However, Wei et al. [14] used first-principles calculation to declare that TiN has a low work function and is easily dissolved during the corrosion process, and TiN inclusion acts as anodes. Their contradictory conclusions confused us. Because of these inconsistent conclusions, it has been proposed that SKPFM test results are negatively correlated with the corrosion behavior [15, 16]. Obviously, SKPFM may not be applicable in some scenarios, and other methods need to be found to detect the potential of the sample.

On the other hand, some researchers use Kernel average misorientation (KAM) diagram to analyze the causes of pitting caused by stress concentration around inclusions [17–19]. Before testing KAM diagram, the sample needs to be stress-annealed. However, if the annealing temperature is too low or too high, stress near the inclusion may not be observed. In addition, the sample preparation requirements are relatively high, which need grinding, mechanical polishing, electrolytic polishing and other processes, and these processes are more complex [20]. During the process of grinding and mechanical polishing, the surface of the sample is prone to stress and mechanical damage, which can lead to a decrease in calibration rate and seriously affect the quality of the collected data. In the electrolysis process, if the time is too short, the electrolysis is not sufficient and the stress is not clearly; if the electrolysis time is too long, it is easy to cause the sample surface to become too black and the inclusion is electrolyzed off [21]. Moreover, due to the existence of different processing software, KAM diagram presentation effect will be different, which will increase the confusion of researchers. Therefore, it is necessary to find other research methods to replace KAM diagram.

At present, first-principles calculations have been widely used in materials. For instance, Liu et al. [22] calculated the elastic modulus of microalloying elements Ce, Ti, V, and Nd in γ -Fe by first-principles calculations. Yang et al. [23] calculated the thermal expansion coefficient of inclusions in steel. However, when the physical and chemical properties of inclusions are calculated by the first-principles calculations method, the calculation results will be very different due to the various crystal structures of inclusions [9, 10] and the selection of different crystal data, which will seriously affect the correctness of the conclusion. Therefore, in order to ensure the accuracy of the calculation results, the selected parameters should be

verified experimentally at the beginning of the calculation. Unfortunately, few authors are devoting the necessary attention to this work.

To solve the above three aspects of problems, in this paper, taking Al₂O₃ inclusions as the research object, we propose some new research methods to analyze such problem. Firstly, the in-situ corrosion morphology of Al₂O₃ inclusions were observed using the field emission scanning electron microscope (FE-SEM). Secondly, the crystal structures of Al₂O₃ inclusion were obtained by electron backscatter diffraction (EBSD) phase identification. Finally, the band structure, work function, and elastic modulus were calculated by first-principles calculations. The thermal expansion coefficients were calculated using Phonopy software. The stress surrounding the inclusion was analyzed by Abaqus software.

2 Methods

2.1 Sample preparation

The tested steel was prepared under laboratory conditions, and its chemical composition is shown in Table 1. The ingot was heated to 1050 °C in the heating furnace, held for 2 h, and then forged. The final rolling temperature was controlled at about 890 °C. The ingot was forged to 30-mm slab and air cooled to room temperature. The samples of 10 mm × 10 mm × 7 mm were prepared, and the work face is a cross section of 10 mm × 10 mm. The work face was first sanded with SiC sandpaper, then polished with polishing agent, and finally cleaned with distilled water and anhydrous ethanol.

2.2 Morphological observation

The morphology of inclusion was observed by FE-SEM. The phase structure of the inclusions was identified by EBSD. The sample for EBSD analysis was first mechanically polished and electrolyzed for 35 s at DC voltage of 22 V in a solution with a volume ratio of ethanol to perchloric acid of 9:1. During the test, the accelerating voltage is 20 kV, the probe current is ~ 5 nA, the working distance is 8.5 mm, and EBSD data are obtained in steps of 1 μ m.

2.3 Immersion test

The simulated seawater corrosion immersion experiment was carried out in 3.5 wt.% NaCl neutral solution (pH = 6.5–7.2), and the samples were taken out after immersion

Table 1 Chemical composition of tested steel (wt.%)

C	Si	Mn	P	S	O	Al _t	N	Ti	Fe
0.0049	0.007	0.12	0.007	0.005	0.0018	0.011	0.003	0.051	Balance

for different time to observe the corrosion morphology. The surface rust layer is removed with descaling liquid and dried for later use. The corrosion morphology of the sample was observed by FE-SEM. The sample after observation was put back into the solution for immersion experiment. After immersion for a period of time, it was taken out and the corrosion morphology of the sample was observed again. The immersion experiment was repeated several time in turn. All immersion experiments were completed at room temperature (25 ± 5 °C).

2.4 Calculation methods

The band structure, surface energy, work function, and elastic modulus of Al₂O₃ inclusion and Fe matrix were calculated by Vienna *ab-initio* simulation package (VASP) software. The thermal expansion coefficient was calculated by Phonopy software. The projector augmented wave (PAW) method was used to describe the interaction between valence electrons and ions when calculating surface energy, work function, and elastic modulus. The exchange correlation interaction between electrons adopted the Perdew–Burke–Ernzerh (PBE) function [24, 25], where the cutoff energy of the plane wave was 450 eV, the Gaussian broadening was 0.05 eV, self-consistent cyclic energy convergence was set to 1.0×10^{-6} eV/atom, and force convergence was 0.02 eV/Å. The *k*-point grids of Fe matrix and Al₂O₃ inclusion were selected as $13 \times 13 \times 13$ and $7 \times 7 \times 2$, respectively.

The distribution of stress concentration around Al₂O₃ inclusion was simulated by Abaqus software. The stress concentration caused by the differences of Young's modulus, thermal expansion coefficient, and Poisson's ratio between Al₂O₃ inclusion and Fe matrix was simulated when the temperature decreased from 890 to 25 °C (room temperature). The selected parameters were derived from first-principles calculations results. The left side of Fe matrix area was fixed in *X* direction and can move freely in *Y* direction. The temperature used the predefined fields in Abaqus/standard. The simulation type was static. During the “seed edge” process, the approximate sizes of Al₂O₃ inclusion and the matrix were set to 0.05 and 0.2, respectively [26].

3 Results and discussion

3.1 Morphology of Al₂O₃ inclusion

FE-SEM images and energy dispersive spectrometry (EDS) elements distribution for inclusions of sample are illustrated in Fig. 1. EDS elemental analysis shows that the type of inclusions is Al₂O₃–TiN. It is elongated, about 10 μm long and 1 μm wide. Moreover, it is worth noting that TiN is attached to Al₂O₃. Some scholars [27] pointed out that due to the brittleness and not easy deformation of Al₂O₃ inclusions, under the action of stress, microcracks are easy to form at the contact between inclusions and the matrix, which is easy to lead to pitting corrosion. However, our results are different from theirs. From Fig. 1, there are no microcracks between Al₂O₃ inclusion and the matrix. Therefore, the cause of pitting corrosion should not be limited to microcracks. Consequently, we need to explore another reason for Al₂O₃ inclusion induced pitting corrosion.

3.2 In-situ corrosion morphology of Al₂O₃ inclusion

In order to better understand the mechanism of pitting corrosion initiation induced by Al₂O₃ inclusion, the in-situ corrosion morphology of the sample (in Fig. 1) was observed, as shown in Fig. 2. It can be seen from Fig. 2a that there is a slight dissolution of the matrix around Al₂O₃ inclusion, resulting in micro-voids between Al₂O₃ and the matrix. Figure 2b is an enlarged view of Fig. 2a, and it can be seen that black cracks appear around Al₂O₃, while no corrosion is found around TiN. Moreover, the initiation of voids is mainly in the areas where Al₂O₃ inclusion contacts the matrix. After immersing for a period of time, the matrix in contact with Al₂O₃ inclusions is further dissolved, resulting in crevices between the inclusion and the matrix, and forming crevice corrosion. At the same time, countless small tiny ripples appear on the matrix far away from inclusion, which means that the matrix also undergoes dissolution, as shown in Fig. 2c. With the further extension of corrosion time, large amounts of matrix in contact with Al₂O₃ inclusion are dissolved, forming deeper corrosion

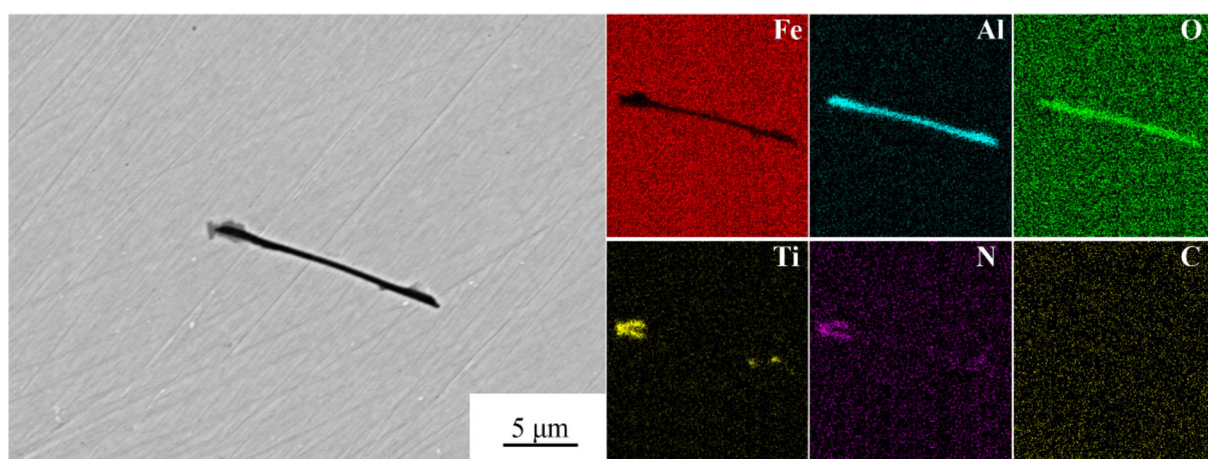


Fig. 1 FE-SEM image and EDS element distribution of inclusion of sample

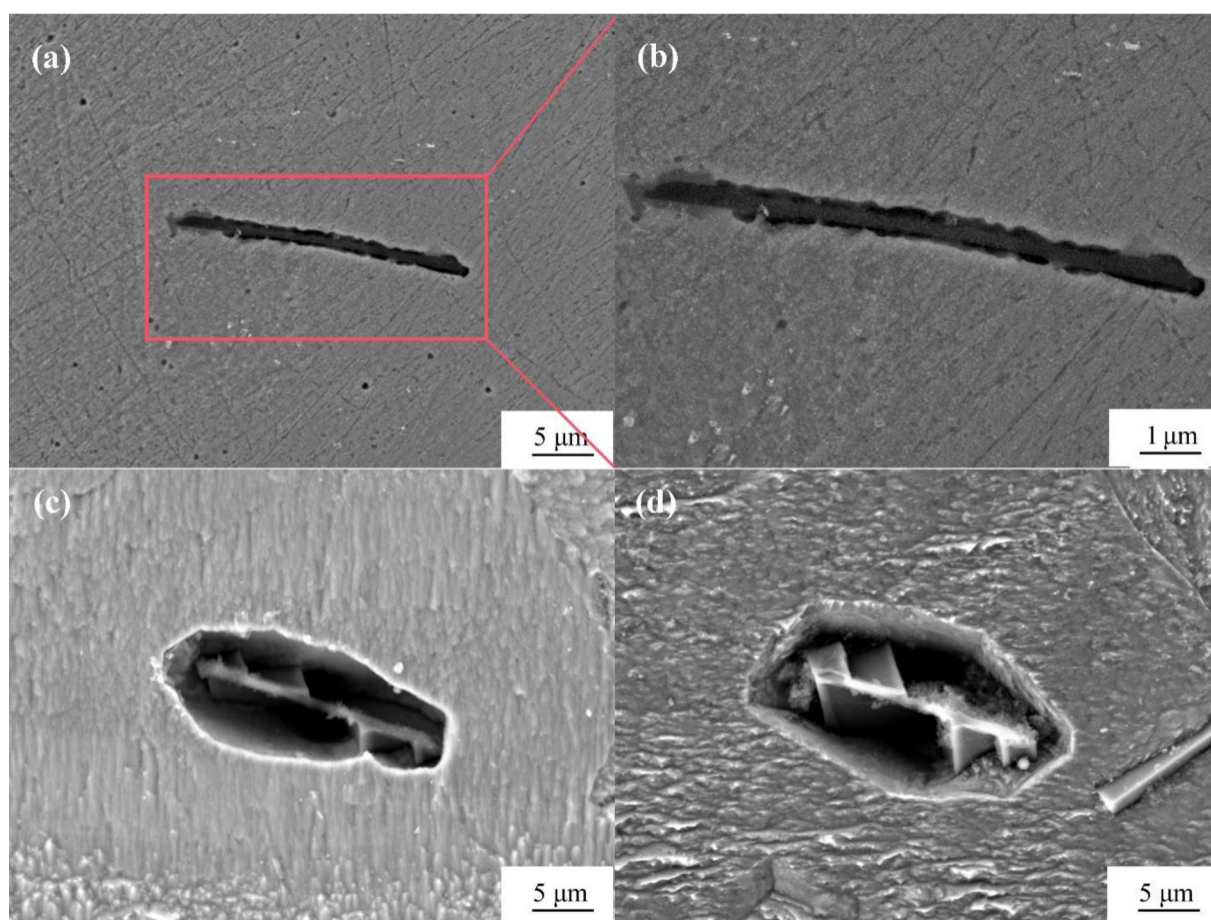


Fig. 2 Microscopic corrosion morphology of Al_2O_3 inclusion. **a** 2 days; **b** enlarged view of **a**; **c** 5 days; **d** 10 days

pits, which are hollow in shape. In addition, it can be found that the corrosion rate of the matrix around Al_2O_3 extends faster in the longitudinal direction than in the transverse direction, indicating that the corrosion pits propagate faster

in the transverse direction than in the longitudinal direction (surface and depth directions of the matrix), as shown in Fig. 2d. From the above analysis, it can be concluded that the matrix prioritizes the dissolution of Al_2O_3 inclusion.

3.3 EBSD phase identification of Al_2O_3 inclusions

To determine the crystal structure of Al_2O_3 inclusion, diffraction analysis and phase identification of the sample were performed by EBSD, and the results are shown in

Fig. 3c. The crystal structure of the inclusion is identified as $\alpha\text{-Al}_2\text{O}_3$ by the Kikuchi diffraction pattern. The space group of the crystal structure is R-3c, as shown in Fig. 3d. The positions of Al and O atoms are (0, 0, 0.148) and (0.306, 0, 0.250), respectively. The lattice parameters are

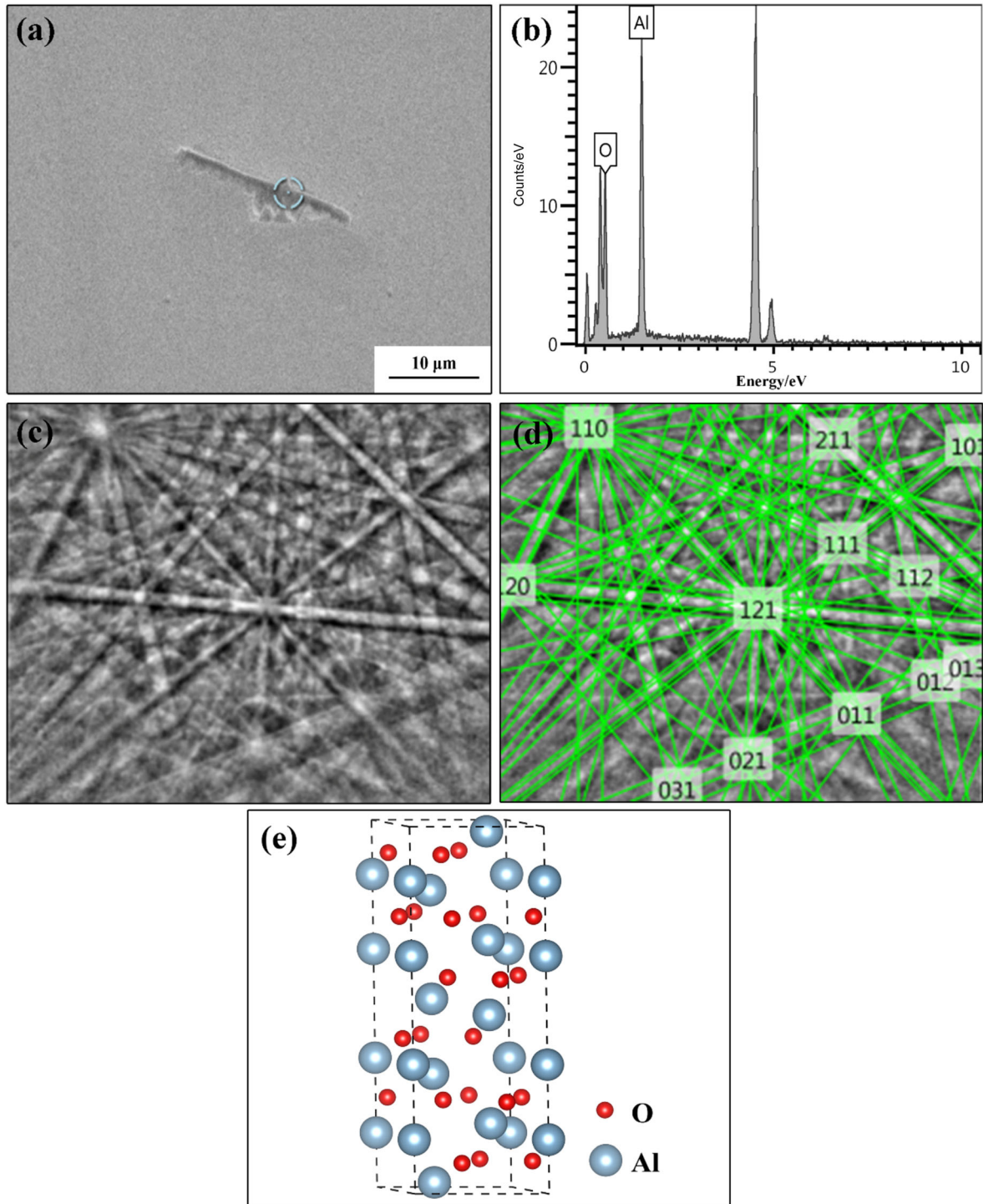


Fig. 3 FE-SEM image of inclusion (a), EDS element distribution of Al_2O_3 inclusion (b), Kikuchi diagram of EBSD testing (c), calibrated diagram (d), and crystal structure of Al_2O_3 inclusion (e)

$a = b = 4.759 \text{ \AA}$, $c = 12.910 \text{ \AA}$, $\alpha = \beta = 90^\circ$, $\gamma = 120^\circ$ [28].

3.4 Simulating calculations

To judge the electrical conductivity of Al_2O_3 inclusion, its band structure is calculated using first-principles calculations. The calculated bandgap of Al_2O_3 is 5.95 eV, as shown in Fig. 4. The experimental value of the bandgap of Al_2O_3 is 5.6 eV [29] and the calculated value is 5.76 eV [30] by others reported in the literature, which shows that our calculated value is within the allowable error range, indicating that the calculation result is reliable and effective. The bandgap of Al_2O_3 is greater than 5 eV [31, 32], indicating that it is an insulator and does not conduct electricity. Therefore, there will be no galvanic corrosion between Al_2O_3 and Fe matrix.

The difference of surface energy (E_{Surf}) and work function (Φ) between inclusions and Fe matrix can affect the current density during the dissolution process [33]. The

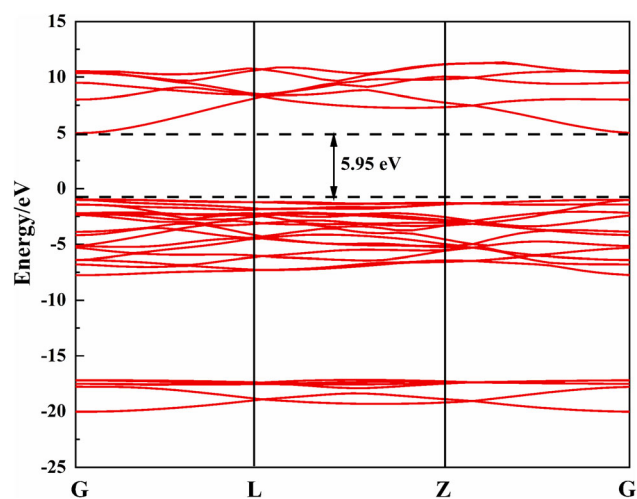


Fig. 4 Band structure of Al_2O_3 inclusion

work function and surface energy of different surfaces of Fe matrix are shown in Table 2. Fe (110) surface has the smallest surface energy, indicating that Fe (110) surface is the most stable, in other words, it has the highest probability of being an exposed surface. Therefore, the work function of Fe (110) surface ($\Phi = 4.711 \text{ eV}$) was chosen as the reference value to compare the work function size of Fe matrix and inclusion. In order to characterize the corrosion tendency of Fe matrix and inclusion, we calculated their work function. The work function can be calculated from Eq. (1).

$$\Phi = V_e - E_F \quad (1)$$

where V_e denotes the electrostatic potential energy of the electron in the vacuum near the surface; and E_F denotes Fermi energy level of the crystal.

The potential difference between the inclusion and Fe matrix (ΔU) can be calculated using Eq. (2).

$$\Delta U = \Phi_{\text{Al}_2\text{O}_3} - \Phi_{\text{Fe}} \quad (2)$$

where $\Phi_{\text{Al}_2\text{O}_3}$ and Φ_{Fe} represent the work function of Al_2O_3 inclusion and Fe matrix, respectively.

The size of the work function reflects the strength of electrons bound in the material. The higher the work function, the more difficult it is for electrons to leave the parent body, and the less susceptible the material is to corrosion [40]. The potential difference between different crystal planes of Al_2O_3 and Fe matrix can be calculated using Eq. (2), and the calculation results are shown in Fig. 5. From Fig. 5, the potential difference between Al_2O_3 (100), (110) and (001) surfaces and Fe matrix is positive, which indicates that the work function of Al_2O_3 (100), (110) and (001) is higher than that of Fe matrix, and it shows that Al_2O_3 is not prone to lose electrons and is not easy to be corroded.

The calculation results of bulk modulus (B), Young's modulus (E), shear modulus (G) and thermal expansion coefficient (α) of Al_2O_3 inclusion and Fe matrix are shown

Table 2 Φ and E_{Surf} of different surfaces of α -Fe

Surface	Terminated plan	Φ/eV			$E_{\text{Surf}}/(\text{J m}^{-2})$		
		Present	DFT [34]	Experiment [35, 36]	Present	DFT [37, 38]	Experiment [39]
100	1	4.452	4.54	4.67	2.501	2.463, 2.470	2.41
	2	4.357	4.54	4.67	2.497	2.429, 2.470	2.41
110	1	4.710	5.12	4.50	2.428	2.645, 2.370	2.41
	2	4.711	5.12	4.50	2.403	2.679, 2.370	2.41
111	1	4.480	4.32	4.81	2.692	2.604, 2.697	2.41
	2	4.483	4.32	4.81	2.685	2.604, 2.697	2.41
	3	4.516	4.32	4.81	2.679	2.605, 2.697	2.41

DFT—Density functional theory

in Fig. 6. From Fig. 6a, there is a significant difference in the elastic modulus between Al₂O₃ inclusion and Fe matrix. *B*, *E* and *G* values of Al₂O₃ are 79.18, 172.59 and 72.95 GPa higher than those of Fe matrix. It can be seen from Fig. 6b that the thermal expansion coefficient of

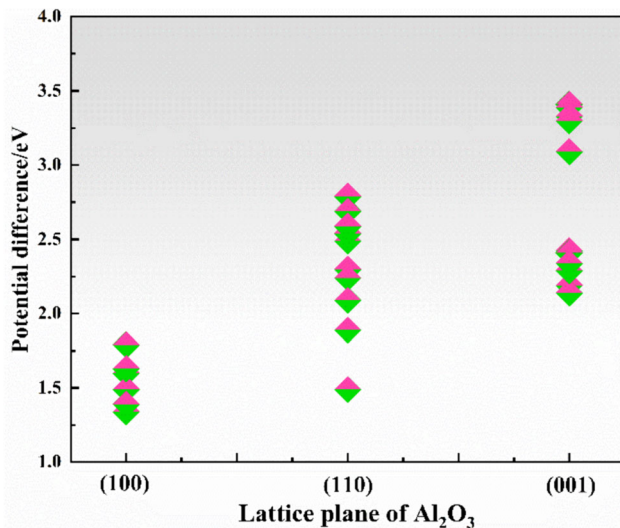


Fig. 5 Potential difference between Al₂O₃ inclusion and Fe matrix

Al₂O₃ is always smaller than that of Fe matrix between 0–800 K. At room temperature (298 K), the thermal expansion coefficient of Al₂O₃ is $8.017 \times 10^{-6} \text{ K}^{-1}$, while that of Fe matrix is $11.724 \times 10^{-6} \text{ K}^{-1}$, indicating that they are quite different (not on the same order of magnitude).

Due to the differences of elastic modulus and thermal expansion coefficient between Al₂O₃ inclusions and Fe matrix, residual stress will be formed between inclusions and matrix during rolling process. When the inclusion is simplified into a sphere, the residual stress around the inclusion can be calculated by Eqs. (3) and (4) [47].

$$\sigma_R = \frac{(\alpha_M - \alpha)\Delta T}{\frac{0.5(1+\nu_M) + (1-2\nu_M)d^3}{E_M(1-d^3)} + \frac{(1-2\nu)}{E}} \quad (3)$$

$$d = \frac{R}{R_M} \quad (4)$$

where α_M , E_M , ν_M represent the thermal expansion coefficient, Young's modulus, and Poisson's ratio of the matrix at room temperature, respectively; ν represents Poisson's ratio of Al₂O₃ inclusion at room temperature; ΔT represents the difference between the hot rolling temperature (890 °C) and the room temperature (25 °C); R is the radius

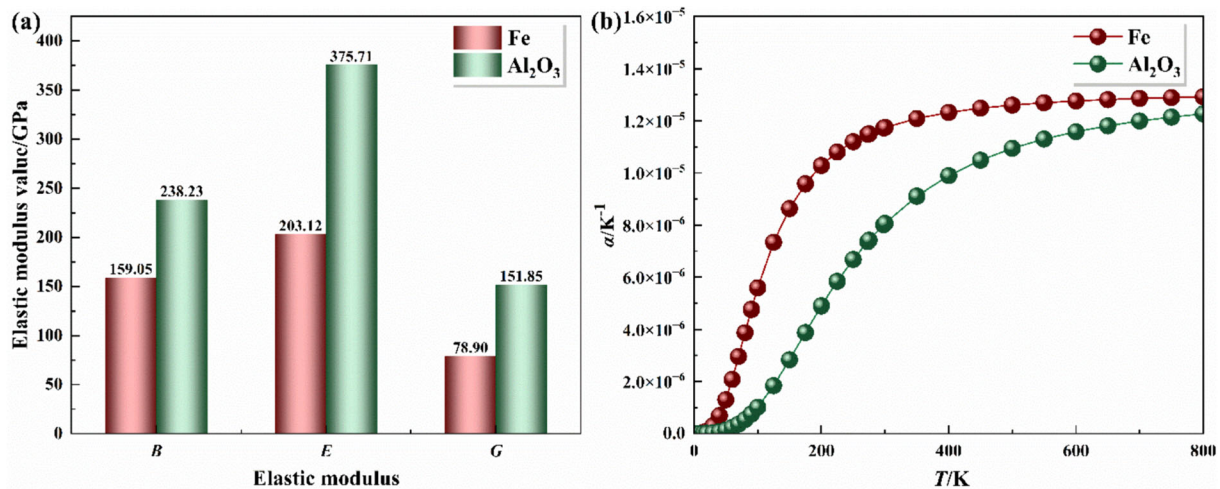


Fig. 6 *B*, *E* and *G* of Fe matrix and Al₂O₃ inclusion (a) and α of Fe matrix and Al₂O₃ inclusion (b)

Table 3 Parameters required for finite element simulations

Parameter	Fe			Al ₂ O ₃		
	Present	Experiment [41, 42]	DFT [43, 44]	Present	Experiment [8, 45]	DFT [23, 46]
<i>E</i> /GPa	203.12	239.00	175.76	375.71	404.60	353.60
α (298 K)/K ⁻¹	11.724×10^{-6}	12.5×10^{-6}	11.724×10^{-6}	8.0169×10^{-6}	8.2×10^{-6}	8.017×10^{-6}
ν	0.30	0.27	0.31	0.24	0.23	0.24

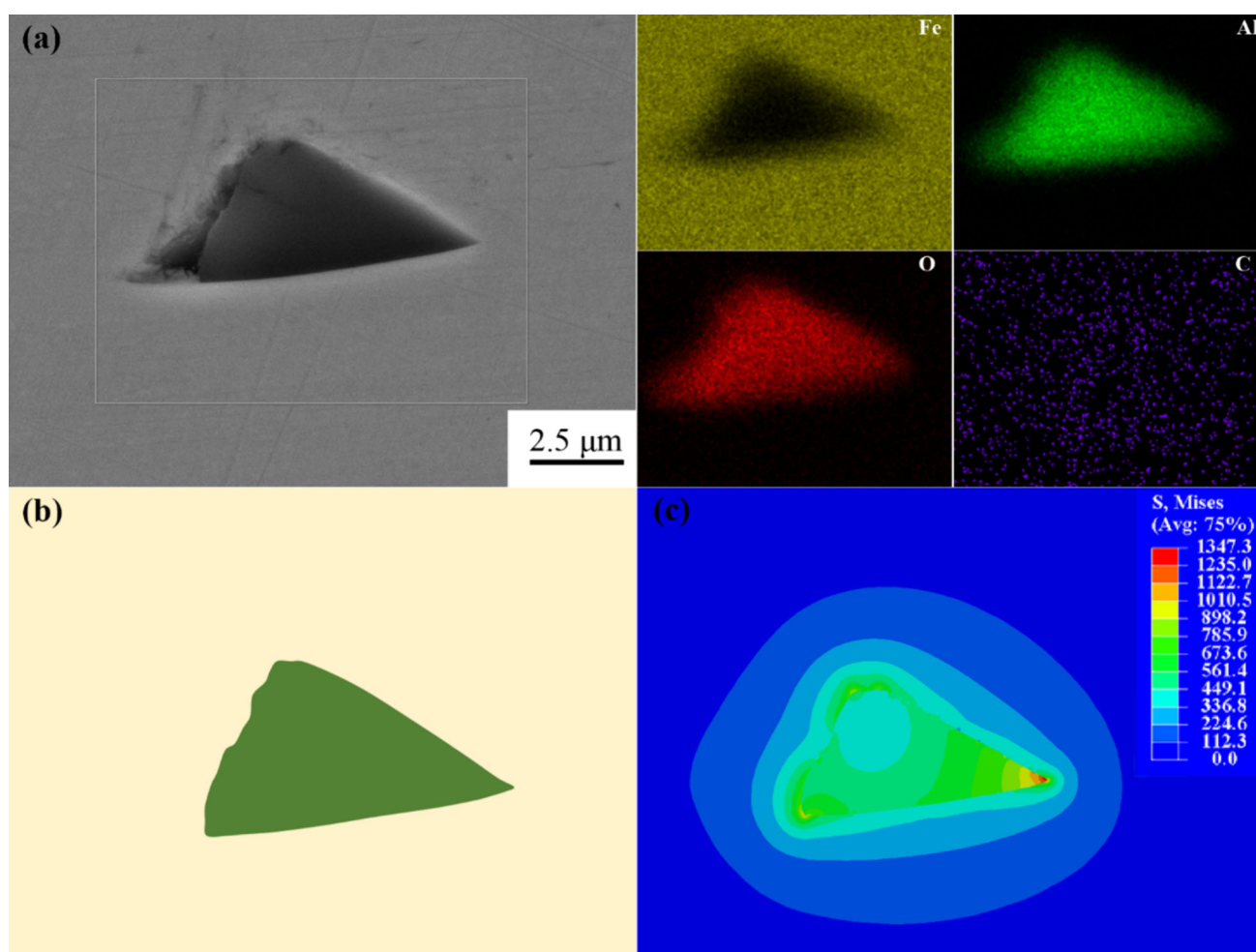


Fig. 7 FE-SEM image of Al₂O₃ inclusion (a), schematic diagram of Al₂O₃ inclusion (b), and simulation results of residual stress distribution around Al₂O₃ inclusion (c)

of the inclusion; R_M is the radius of the matrix around Al₂O₃ inclusion; d is ratio of the radius of the matrix around the inclusion to the radius of the inclusion, assuming 4 [48]; and σ_R is the amount of residual stress. The parameters selected in Eqs. (3) and (4) are derived from first-principles calculations results, and the data are listed in Table 3. According to Eqs. (3) and (4), the maximum calculated residual stress around Al₂O₃ inclusion is 724.66 MPa.

Because Al₂O₃ inclusion is a hard and brittle phase, in the hot rolling process, the inclusions at the sharp corners are easy to extrude to the matrix, forming residual stress. The residual stress distribution around Al₂O₃ inclusion was simulated by Abaqus software, and the results are shown in Fig. 7. The residual stress at the sharp corner of the inclusion is relatively large, and it decreases with the increase in the distance from the inclusions. The maximum residual stress is 785.9 MPa, which is slightly greater than the calculated value (but still within an acceptable range).

This may be because the Abaqus software optimizes the shape of the inclusions during simulation.

EBSD can characterize the degree of lattice distortion in the matrix around inclusions, KAM diagram can qualitatively measure the degree of lattice distortion in adjacent areas of inclusions [49]. EBSD test results of the sample are shown in Fig. 8. In KAM diagram, the degree of lattice distortion increases in order of blue, green, yellow, and red. From Fig. 8c, there are a large number of green areas and a small amount of yellow and red areas around Al₂O₃, indicating a significant high-density lattice distortion (stress concentration) area in the matrix around Al₂O₃. During the corrosion process, this area has high activity and is prone to dissolution. This can be used to explain why the matrix in contact with Al₂O₃ inclusions preferentially dissolves during the corrosion process.

There are two main reasons for the formation of lattice distortion areas in the matrix around Al₂O₃ inclusions: (1) The crystal type of Al₂O₃ inclusion is trigonal system, and while the crystal type of Fe matrix is a cubic system, these

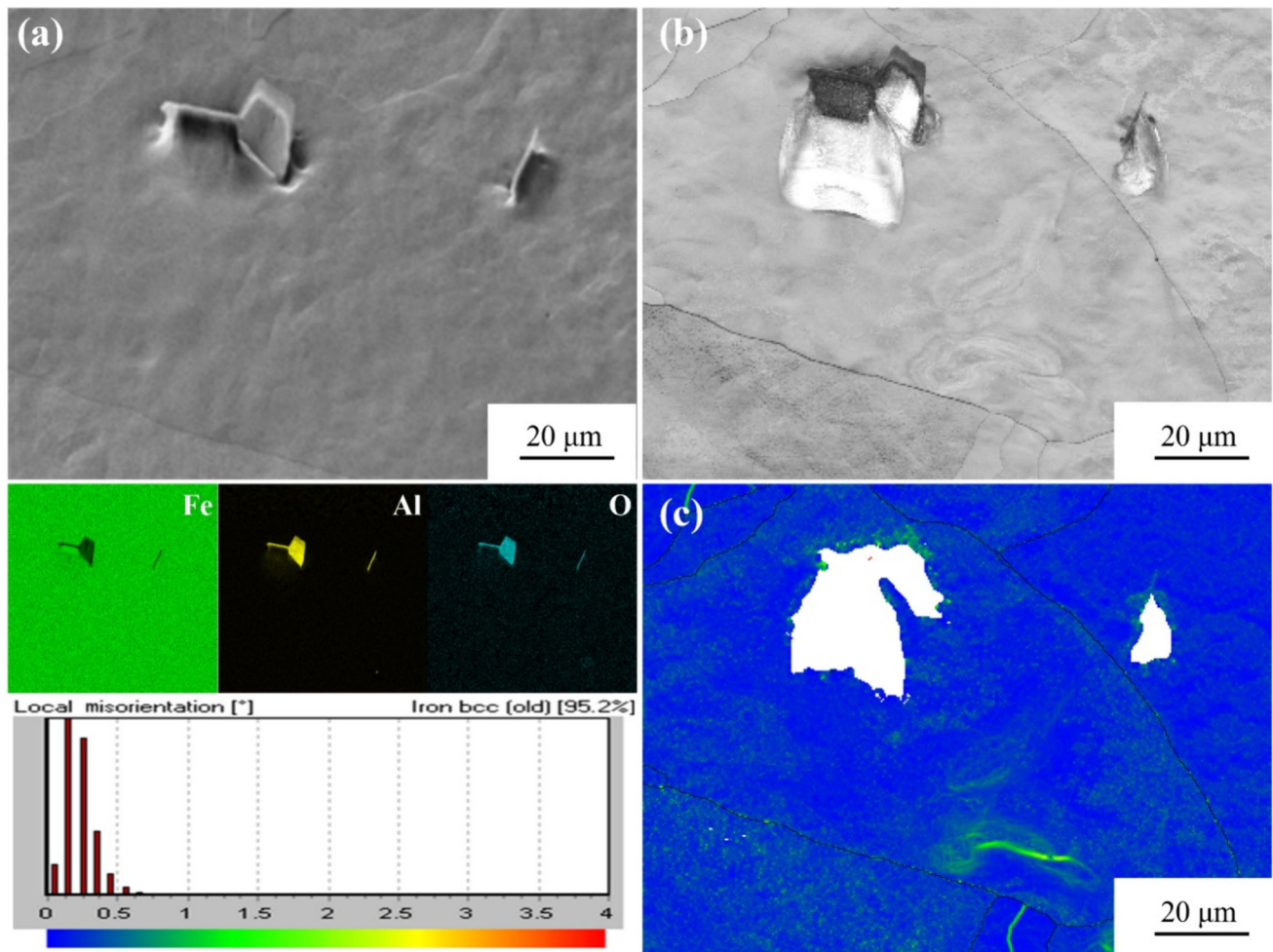


Fig. 8 EBSD test results of Al₂O₃ inclusion. **a** FE-SEM image; **b** chart with contrast; **c** KAM diagram of target areas

two different crystal structures cannot form coherent or semi coherent interfaces. Therefore, the interface formed between the two has high energy and poor stability. (2) There is a significant difference in the elastic modulus and thermal expansion coefficient between Al₂O₃ inclusions and Fe matrix, which leads to significant internal stress at the interface between the two during the hot rolling process.

3.5 Origin mechanism of pitting initiated by Al₂O₃ inclusion

From the above analysis, Al₂O₃ is an insulator, so that it will not cause galvanic coupling corrosion. Figure 9 shows the schematic diagram of corrosion process induced by Al₂O₃ inclusions. After immersion for a short period of time, there is a micro-gap between Al₂O₃ inclusions and the matrix, while Cl⁻ or aggressive solution enters the micro-gap and continues to corrode the matrix, forming crevice corrosion [32], as shown in Fig. 9a. According to

the results of first-principles calculations and KAM diagrams, there is a clear stress concentration area around Al₂O₃ inclusion, which means that there is a significant lattice distortion area at the interface between Al₂O₃ and the matrix [27, 50], as shown in the green section in Fig. 9a. This part of the matrix has relatively high electrochemical activity and is easily hydrolyzed. Therefore, micro-coupling corrosion is formed between the matrix in the high-density lattice distortion area around Al₂O₃ inclusions and the matrix in the non-distortion area. The matrix in the high-density lattice distortion area acts as an anode and the matrix in the non-lattice distortion area acts as a cathode [11], where electrochemical reactions occur. As corrosion progresses, the matrix in the high-density lattice distortion area undergoes an anodic dissolution reaction. At the same time, a small amount of corrosion products are generated on the inclusions and accumulated above them, as shown in Fig. 9b. When the matrix in the lattice distortion area is completely dissolved, the accumulated corrosion products make it difficult to exchange

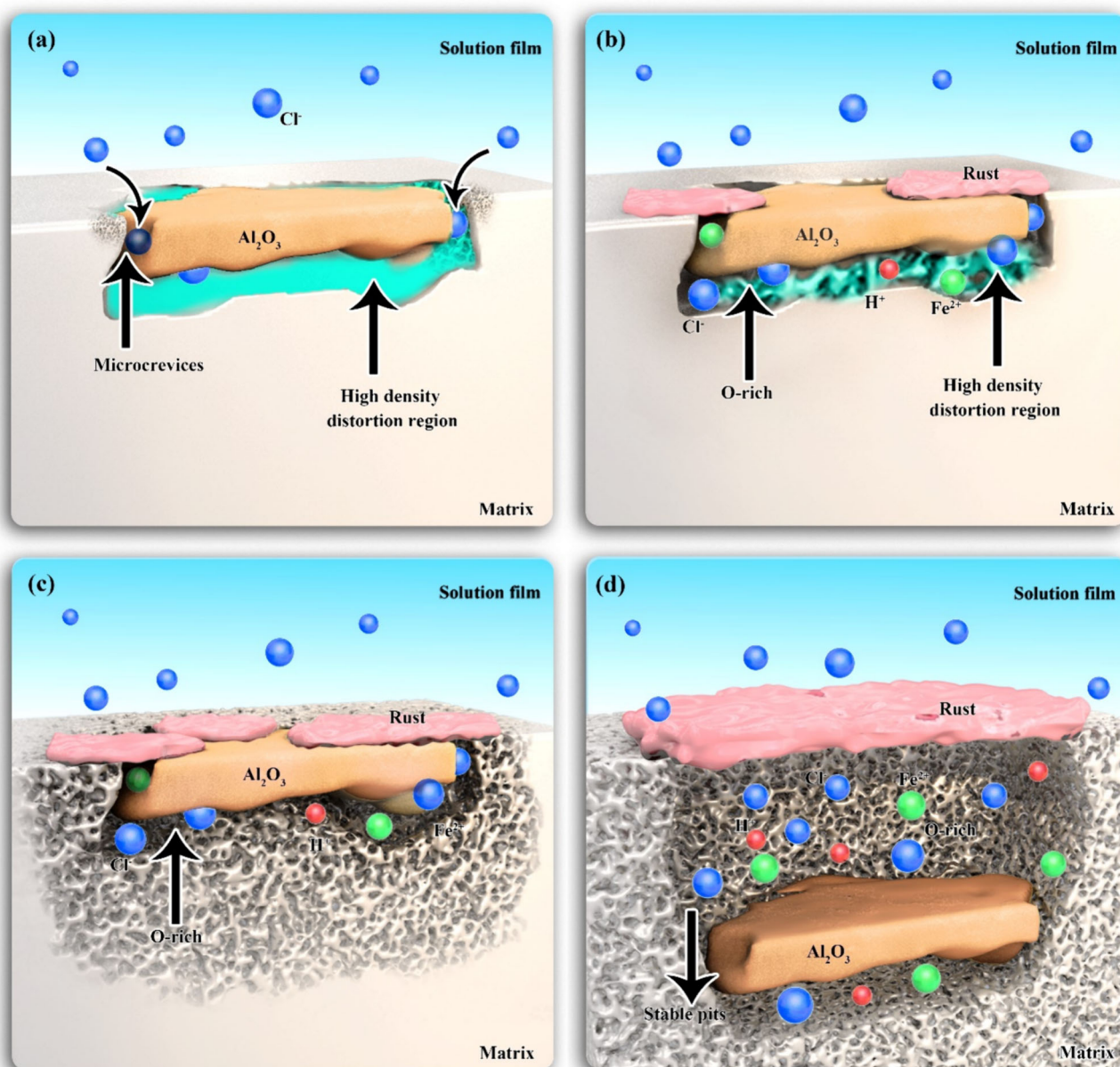


Fig. 9 Schematic diagram of pitting initiation and propagation induced by Al_2O_3 inclusion

substances inside and outside the corrosion pit. At this point, O_2 concentration inside the corrosion pit is lower than that outside the pit, thus forming an oxygen concentration difference battery [51], which makes the matrix inside the pit be continuously ionized and Fe^{2+} concentration increase. To maintain the electrical neutrality of the solution inside the pit, Cl^- outside the pit migrates into the hole and forms a soluble salt with Fe^{2+} . The increasing concentration of Cl^- in the pit accelerates the hydrolysis reaction of Fe^{2+} : $\text{Fe}^{2+} + 2\text{H}_2\text{O} \rightarrow \text{Fe}(\text{OH})_2 + 2\text{H}^+$, as

shown in Fig. 9c. As the reaction occurs further, H^+ concentration gradually increases and pH gradually decreases, making the pit be severely acidified and forming a closed acidified autocatalytic battery [52, 53]. Accelerating the dissolution rate of the matrix in the pit makes the corrosion pit expand to the depth and finally form a deeper pitting pit [27, 54], as shown in Fig. 9d.

In the process of corrosion, the corrosion pit grows continuously under the combined effect of self-corrosion current in the occluded areas and anodic polarization

current, which promotes further corrosion. The severe acidification environment of the corrosion pit will promote the dissolution reactions of Al₂O₃ inclusions [55–57]. Therefore, during the observation of corrosion morphology, because Al₂O₃ inclusions completely dissolved or peeled off the matrix, Al₂O₃ inclusions were not found in some corrosion pits.

4 Conclusions

1. Al₂O₃ inclusion is an insulator and non-conductive, and there is no galvanic corrosion between Al₂O₃ inclusion and the matrix. The work function of Al₂O₃ is greater than that of Fe matrix, which makes it difficult to lose electrons and dissolve during corrosion reactions. The stress concentration of the matrix around Al₂O₃ inclusions is relatively high, and then, the high and the low stress concentration areas formed a micro-galvanic corrosion, which can be used to explain the reason of the pitting induced by Al₂O₃ inclusions.
2. The pitting behavior of inclusions can be analyzed by calculating the band structure and work function. In addition, the method of first-principles calculations coupled with finite element simulation can be used to characterize the stress concentration around inclusions. The calculation methods have the potential to be extended to study the pitting corrosion of common inclusions in steel.

Acknowledgements This work was supported by the National Natural Science Foundation of China (Nos. 52364044 and 52204364), Central Guidance on Local Science and Technology Development Fund Projects of Inner Mongolia Autonomous Region (No. 2022ZY0090), and Basic Scientific Research Business Expenses of Colleges and Universities in Inner Mongolia Autonomous Region (Nos. 2023QNJS011 and 0406082226).

Declarations

Conflict of interest The authors declare no conflict of interest.

References

- [1] X. Li, D. Zhang, Z. Liu, Z. Li, C. Du, C. Dong, *Nature* 527 (2015) 441–442.
- [2] B. Hou, X. Li, X. Ma, C. Du, D. Zhang, M. Zheng, W. Xu, D. Lu, F. Ma, *NPJ Mater. Degrad.* 1 (2017) 4.
- [3] S. Yang, Z. Che, W. Liu, Z. Liu, W. Liu, X. Cheng, C. Liu, X. Li, *Corros. Sci.* 225 (2023) 111610.
- [4] X. Liu, C. Yang, H. Ren, Y. Li, Z. Jin, F. Zhang, J. Yang, *J. Rare Earths* 41 (2023) 1448–1458.
- [5] Z. Pu, X. Chen, X. Meng, Y. Wu, L. Shen, Q. Wang, T. Liu, M. Shuai, *Corros. Sci.* 124 (2017) 160–166.
- [6] G. Li, L. Wang, H. Wu, C. Liu, X. Wang, Z. Cui, *Corros. Sci.* 174 (2020) 108815.
- [7] J. Villavicencio, N. Ulloa, L. Lozada, M. Moreno, L. Castro, *J. Mater. Res. Technol.* 9 (2020) 5894–5911.
- [8] L.W. Wang, J.C. Xin, L.J. Cheng, K. Zhao, B.Z. Sun, J.R. Li, X. Wang, Z.Y. Cui, *Corros. Sci.* 147 (2019) 108–127.
- [9] Z. Li, Y. Ji, J. Chen, C. Yin, J. Song, K. Xiao, *J. Mater. Res. Technol.* 24 (2023) 2469–2481.
- [10] C. Liu, R.I. Revilla, X. Li, Z. Jiang, S. Yang, Z. Cui, D. Zhang, H. Terryn, X. Li, *J. Mater. Sci. Technol.* 124 (2022) 141–149.
- [11] C. Liu, X. Li, R.I. Revilla, T. Sun, J. Zhao, D. Zhang, S. Yang, Z. Liu, X. Cheng, H. Terryn, X. Li, *Corros. Sci.* 179 (2021) 109150.
- [12] E. Bettini, U. Kivisäkk, C. Leygraf, J. Pan, *Electrochim. Acta* 113 (2013) 280–289.
- [13] W. Xue, Z.L. Li, K. Xiao, W. Yu, J.L. Song, J.H. Chen, C.F. Dong, X.G. Li, *Corros. Sci.* 163 (2020) 108232.
- [14] W. Wei, K. Wu, X. Zhang, J. Liu, P. Qiu, L. Cheng, *J. Mater. Res. Technol.* 9 (2020) 1412–1424.
- [15] M. Iannuzzi, K.L. Vasanth, G.S. Frankel, *J. Electrochem. Soc.* 164 (2017) C488–C497.
- [16] R.H. Buzolin, M. Mohedano, C.L. Mendis, B. Mingo, D. Tolnai, C. Blawert, K.U. Kainer, H. Pinto, N. Hort, *Mater. Sci. Eng. A* 682 (2017) 238–247.
- [17] Y. Yang, T. Zhang, Y. Shao, G. Meng, F. Wang, *Corros. Sci.* 73 (2013) 250–261.
- [18] Y. Wang, X. Zhang, L. Cheng, J. Liu, T. Hou, K. Wu, *J. Mater. Res. Technol.* 13 (2021) 2419–2432.
- [19] S. Tokuda, I. Muto, Y. Sugawara, N. Hara, *Corros. Sci.* 183 (2021) 109312.
- [20] S.H. Shin, S.I. Lee, B. Hwang, *Mater. Charact.* 206 (2023) 113418.
- [21] K.C. Sahoo, S. Goyal, V.T. Paul, K. Laha, *Mater. High Temp.* 37 (2020) 295–304.
- [22] X.J. Liu, J.C. Yang, C.K. Cai, A.X. Li, X. Lei, C.Q. Yang, *Steel Res. Int.* 92 (2021) 2100053.
- [23] C. Yang, X. Liu, J. Yang, Q. Yang, *Metall. Res. Technol.* 119 (2022) 503.
- [24] S. Khalid, Y. Ma, X. Sun, G. Zhou, H. Wu, G. Lu, Z. Yang, J. Khan, R. Khenata, A. Bouhemadou, *J. Mater. Res. Technol.* 9 (2020) 413–420.
- [25] Y. Yang, X.Z. Dai, X.R. Yang, S.H. Zhang, D.Y. Li, *Acta Mater.* 196 (2020) 347–354.
- [26] W. Cheng, B. Song, J. Mao, *Int. J. Hydrog. Energy* 48 (2023) 15303–15316.
- [27] C. Liu, R.I. Revilla, D. Zhang, Z. Liu, A. Lutz, F. Zhang, T. Zhao, H. Ma, X. Li, H. Terryn, *Corros. Sci.* 138 (2018) 96–104.
- [28] Y. Liu, Y. Huang, Z. Xiao, C. Yang, X. Reng, *Int. J. Mod. Phys. B* 30 (2016) 1650085.
- [29] M.A. Konyushenko, E.O. Filatova, A.S. Konashuk, A.V. Nelyubov, A.S. Shulakov, *Tech. Phys. Lett.* 41 (2015) 922–925.
- [30] J. Zhang, C. Su, X. Chen, H. Liu, L. Zhang, *Mater. Today Commun.* 27 (2021) 102204.
- [31] Y. Hou, G. Xiong, L. Liu, G. Li, N. Moelans, M. Guo, *Scripta Mater.* 177 (2020) 151–156.
- [32] J.Z. Hu, S. Li, J. Zhang, Y. Ren, L.F. Zhang, *J. Iron Steel Res. Int.* (2023) <https://doi.org/10.1007/s42243-023-01101-5>.
- [33] H. Ma, X.Q. Chen, R. Li, S. Wang, J. Dong, W. Ke, *Acta Mater.* 130 (2017) 137–146.
- [34] M. Tang, K. Wu, J. Liu, L. Cheng, X. Zhang, Y. Chen, *Materials* 12 (2019) 3359.
- [35] H.L. Skriver, N.M. Rosengaard, *Phys. Rev. B* 46 (1992) 7157–7168.
- [36] A.W. Dweydari, C.H.B. Mee, *Phys. Stat. Sol.* 27 (1975) 223–230.

- [37] Y. Hou, J. Wang, L. Liu, G. Li, D. Zhai, *Micron* 138 (2020) 102898.
- [38] H.B. Michaelson, *J. Appl. Phys.* 48 (1977) 4729–4733.
- [39] W.R. Tyson, W.A. Miller, *Surf. Sci.* 62 (1977) 267–276.
- [40] D.P. Ji, Q. Zhu, S.Q. Wang, *Surf. Sci.* 651 (2016) 137–146.
- [41] C. Kittel, P. McEuen, *Introduction to solid state physics*, Wiley, New York, USA, 1986.
- [42] M. Ellner, I. Park, *Metall. Mater. Trans. A* 33 (2002) 3591–3595.
- [43] X.Q. Li, J.J. Zhao, J.C. Xu, *Front. Phys.* 7 (2012) 360–365.
- [44] X. Liu, J. Yang, F. Zhang, X. Fu, H. Li, C. Yang, *J. Rare Earths* 39 (2021) 477–486.
- [45] S. Davis, G. Gutiérrez, *J. Phys. Condens. Mater.* 23 (2011) 495401.
- [46] H. Yao, L. Ouyang, W.Y. Ching, *J. Am. Ceram. Soc.* 90 (2007) 3194–3204.
- [47] C. Gu, J. Lian, Y. Bao, W. Xiao, S. Münstermann, *Appl. Sci.* 9 (2019) 455.
- [48] H. Xiao, F. Huang, Z. Peng, L. Fan, J. Liu, *Corros. Sci.* 195 (2022) 110006.
- [49] N. Saeidi, F. Ashrafzadeh, B. Niroumand, F. Barlat, *Mater. Des.* 87 (2015) 130–137.
- [50] H. Ma, Z.X. Wang, Y. Liu, Y.X. Wang, T.F. Wang, Q.P. Zhang, Z.Y. Cui, *J. Iron Steel Res. Int.* 30 (2023) 2067–2079.
- [51] W.Z. Wei, K.M. Wu, J. Liu, L. Chen, X. Zhang, *J. Iron Steel Res. Int.* 28 (2021) 453–463.
- [52] Q. Xu, K. Gao, W. Lv, X. Pang, *Corros. Sci.* 102 (2016) 114–124.
- [53] C. Liu, R.I. Revilla, Z. Liu, D. Zhang, X. Li, H. Terryn, *Corros. Sci.* 129 (2017) 82–90.
- [54] L. Yue, Y. Meng, J. Han, K. Xie, Y. Sun, Y. Tan, *J. Rare Earths* 41 (2023) 321–330.
- [55] C.P. O’Hagan, B.J. O’Brien, S.B. Leen, R.F.D. Monaghan, *Corros. Sci.* 109 (2016) 101–114.
- [56] M.A. Baker, J.E. Castle, *Corros. Sci.* 34 (1993) 667–682.
- [57] C.S. Brossia, R.G. Kelly, *Corros. Sci.* 40 (1998) 1851–1871.

Springer Nature or its licensor (e.g. a society or other partner) holds exclusive rights to this article under a publishing agreement with the author(s) or other rightsholder(s); author self-archiving of the accepted manuscript version of this article is solely governed by the terms of such publishing agreement and applicable law.